Observing and modeling the sequential pairwise reactions that drive solid-state ceramic synthesis

Akira Miura*, Christopher J. Bartel, Yusuke Goto, Yoshikazu Mizuguchi, Chikako Moriyoshi, Yoshihiro Kuroiwa, Yongming Wang, Toshie Yaguchi, Manabu Shirai, Masanori Nagao, Nataly Carolina Rosero-Navarro, Kiyoharu Tadanaga, Gerbrand Ceder, Wenhao Sun*

Prof. A. Miura[+], Prof. N.C. Rosero-Navarro, Prof. K. Tadanaga

Faculty of Engineering, Hokkaido University, Sapporo 060-8628, Japan

Dr. C. Bartel[+], Prof. G. Ceder

Department of Materials Science and Engineering, UC Berkeley, Berkeley, California 94720, USA

Materials Sciences Division, Lawrence Berkeley National Laboratory, Berkeley, CA 94720, USA

Prof. Y. Goto, Prof. Y. Mizuguchi

Department of Physics, Tokyo Metropolitan University, Hachioji 192-0397, Japan

Prof. C. Moriyoshi, Prof. Y. Kuroiwa

Graduate School of Advanced Science and Engineering, Hiroshima University, 1-3-1 Kagamiyama, Higashihiroshima, 739-8526, Japan

Prof. Y. Wang

Creative Research Institution Hokkaido University, Kita 21, Nishi 10, Sapporo 001-0021, Japan

Dr. T. Yaguchi, Dr. M. Shirai

Hitachi High-Tech Corporation, Ichige 882 Hitachinaka, 312-8504 Japan

Prof. M. Nagao

Center for Crystal Science and Technology, University of Yamanashi, Kofu 400-8511, Japan

Prof. W. Sun

Department of Materials Science and Engineering, University of Michigan, Ann Arbor, Michigan, 48109, USA

[+] These authors contributed equally.

Email: amiura@eng.hokudai.ac.jp, whsun@umich.edu

Keywords: predictive synthesis, ceramics, in-situ XRD, in-situ TEM, DFT, $YBa_2Cu_3O_{6+x}$

Solid-state synthesis from powder precursors is the primary processing route to advanced multicomponent ceramic materials. Designing reaction conditions and precursors for ceramic synthesis can be a laborious, trial-and-error process, as heterogeneous mixtures of precursors often evolve through a complicated series of reaction intermediates. Here, we use *ab initio* thermodynamics to model which pair of precursors has the most reactive interface, enabling us to understand and anticipate which non-equilibrium intermediates form in the early stages of a solid-state reaction. Using *in situ* X-ray diffraction and *in situ* electron microscopy, we observe how these initial intermediates influence phase evolution in the synthesis of the classic high-temperature superconductor $YBa_2Cu_3O_{6+x}$ (YBCO). Our model rationalizes how the replacement of the traditional $BaCO_3$ precursor with BaO_2 redirects phase evolution through a low-temperature eutectic melt, facilitating the formation of YBCO in 30 minutes instead of 12+ hours. Precursor selection plays an important role in tuning the thermodynamics of interfacial reactions and emerges as an important design parameter in the planning of kinetically favorable synthesis pathways to complex ceramic materials.

Solid-state ceramic synthesis involves heating a mixture of precursor powders at high temperatures (typically >700 °C) and has been used to realize countless functional materials [1-3]. Recent *in situ* characterization studies have revealed that solid-state reactions often evolve through a variety of non-equilibrium intermediates prior to formation of the equilibrium phase [4-10]. These complicated phase evolution sequences are currently difficult to understand, resulting in laborious trial-and-error efforts to optimize ceramic synthesis recipes. Theory and computation could help guide synthesis planning, but computation has mostly been used to evaluate thermodynamic stability or overall reaction energies [11-16]. While these quantities are valuable, they do not provide mechanistic insights into which non-equilibrium intermediates will appear during phase evolution. The ability to rationalize and anticipate which intermediate phases form would enable solid-state chemists to design crystallization pathways that target (or avoid) specific intermediates, accelerating the design of time- and energy-efficient ceramic synthesis recipes for new materials.

The complexity of phase evolution in solid-state synthesis arises from the various pathways by which an initially heterogeneous mixture of precursor particles can transform to a homogeneous target phase. At the microscopic level, solid-state reactions initiate in the interfacial regions between precursors as the system is heated. Because interfacial reactions can only occur between two solid phases at a time, we hypothesize that by determining which pair of precursors exhibits the most reactive interface, we can anticipate which interfacial reaction initiates the overall solid-state reaction, as illustrated schematically in **Figure 1a**. Once two precursors react to form a new phase, this non-equilibrium intermediate will then react through its interface with other precursors and intermediate phases. By decomposing the overall phase evolution into a sequence of pairwise reactions, we can calculate the thermodynamics and analyze the kinetics of each reaction

step separately, providing a simplified theoretical picture to conceptualize and navigate ceramic synthesis [15, 17-20].

We demonstrate how this concept of sequential pairwise reactions enables us to model phase evolution in the ceramic synthesis of the classic high-temperature superconductor, $YBa_2Cu_3O_{6+x}$ (YBCO) [21-23]. Following the discovery that YBCO remains superconducting above the boiling point of liquid N_2 (>77 K), YBCO has been synthesized many thousands of times in laboratories around the world. The typical synthesis recipe for YBCO calls for three precursors—a 0.5/2/3 molar ratio of Y_2O_3/$BaCO_3$/CuO powders—which are ground in a mortar, then compacted, pelletized, and baked in air at 950 °C for >12 hours. Even after 12 hours, the synthesis reaction is often incomplete, so the pellets must be re-ground, re-pelletized, and re-baked until phase-pure YBCO is obtained [24].

It has been reported that replacing $BaCO_3$ with BaO_2 can shorten YBCO synthesis times to 4 hours and eliminate the need for regrinding [25, 26]. This dramatic difference in synthesis times offers an ideal case study to explore how precursor selection governs phase evolution in solid-state synthesis [27]. In **Figure 1b**, we show temperature-dependent Gibbs reaction energies, ΔG_{rxn}, for the formation of YBCO with either BaO_2 or $BaCO_3$ as the barium source. BaO_2 is less stable than $BaCO_3$ [28], so although both reactions are thermodynamically favorable ($\Delta G_{rxn} < 0$) above ~700 °C, the thermodynamic driving force (magnitude of ΔG_{rxn}) is much larger with BaO_2.

Naively, one might anticipate that this larger driving force explains why YBCO synthesis with a BaO_2 precursor proceeds faster. Here, we show that the mechanism actually proceeds in multiple stages. First, the BaO_2 precursor initiates an early BaO_2|CuO reaction to form a crucial $Ba_2Cu_3O_6$ intermediate. This intermediate then directs phase evolution through a low-temperature eutectic

melt, which provides fast liquid diffusion to facilitate rapid YBCO formation in only 30 minutes. BaO_2 is a relatively uncommon YBCO precursor, appearing in only 8 out of 237 synthesis recipes for YBCO (and related phases) as text-mined from the literature [29], whereas $BaCO_3$ is the most common Ba precursor, at 176 out of 237 recipes (all extracted synthesis recipes are shown in **Table S1**). By better understanding how uncommon precursors promote kinetically favorable sequential pairwise reactions [27], we can build towards new design principles for precursor selection and rational synthesis planning.
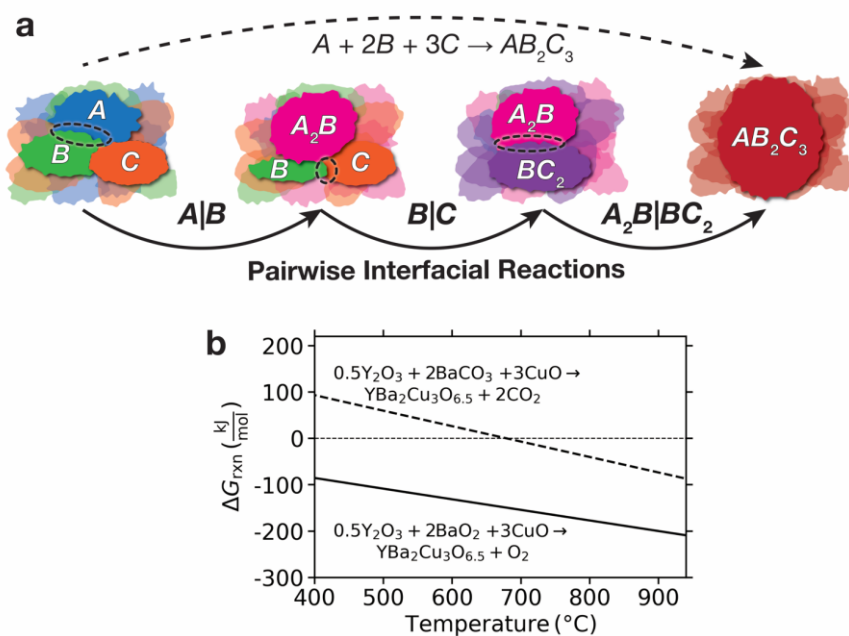
Figure 1. Schematic of sequential pairwise interfacial reactions and overall reaction energetics for YBCO synthesis. (a) Schematic of the pairwise reaction concept, illustrating that phase evolution from powder precursors must initiate at the shared interface between two precursor grains. **(b)** The temperature-dependent Gibbs reaction energies, ΔG_{rxn}, for the formation of YBCO from precursor mixtures utilizing $BaCO_3$ (dashed line) or BaO_2 (solid line) as the Ba source.

Here, we use *in situ* synchrotron X-ray diffraction (XRD) to characterize the temperature-time-transformation process of YBCO formation, as well as *in situ* microscopy (SEM, DF-STEM) to directly observe the spatiotemporal microstructural evolution from the three initial precursors. By comparing these experimentally observed phase evolution pathways against density functional theory (DFT)-calculated thermodynamics [30] aided by a machine-learned model for temperature-dependent Gibbs free energies [31], we both model and observe the role of interfacial reactions in dictating phase evolution in solid-state synthesis. In particular, we show how thermodynamic calculations can predict the relative reactivity of pairwise interfaces, and can also anticipate the first intermediate that forms at the most reactive interface. Once this first intermediate forms, kinetically controlled processes play a more significant role in the subsequent phase evolution, which is directly observed using *in situ* characterization. Our work here provides a theoretical foundation to model phase evolution from multiple precursors and demonstrates the importance of precursor selection in governing the dynamics of phase evolution during the solid-state synthesis of complex ceramics.

In **Figure 2**, we show *in situ* synchrotron X-ray diffraction patterns for phase evolution in YBCO synthesis in air with either $BaCO_3$ (**Figure 2a**) or BaO_2 (**Figure 2b**) as the Ba source, which we compare to the thermodynamic driving force for new phase formation at each pairwise interface (**Figure 2c-d**). **Figure 2a** shows that when $BaCO_3$ is used, the precursors remain the dominant phases up to 940 °C, confirming the lack of rapid phase formation. In contrast, **Figure 2b** shows the formation of $YBa_2Cu_3O_6$ in 30 min when BaO_2 is used as the Ba source. The XRD peaks are sharper at the end of the experiment, suggesting a significant increase in the size of coherently scattering crystallites in the product phases (see **Figure S2**). At the end of heating, a small amount of Y_2BaCuO_5 impurity was also formed (~6% impurity by Rietveld analysis).

We have three-precursor systems in both *in situ* experiments, so the relevant interfaces are $Y_2O_3|CuO$, $Y_2O_3|BaCO_3(BaO_2)$, and $BaCO_3(BaO_2)|CuO$. In the $BaCO_3$-containing system, no reaction has substantial driving force until >900 °C (**Figure 2c**). When $BaCO_3$ is replaced with BaO_2, the reaction thermodynamics change dramatically as the $BaO_2|CuO$ interface has large driving force ($\Delta G_{rxn} < -200$ kJ/mol) to form ternary Ba-Cu-oxides above 400 °C (**Figure 2d**). This is consistent with *in situ* XRD observations of barium copper oxides emerging at ~600 °C and the consumption of BaO_2 by ~700 °C (**Figure 2b**).

Synthesis of YBCO using a $BaCO_3$ precursor usually requires >12 hours with intermittent re-grindings [24], so it is not surprising that YBCO did not form in our 30 min *in situ* experiment (**Figure 2a**). At temperatures >850 °C, traces of a $Y_2Cu_2O_5$ phase are observed, even though the $BaCO_3|CuO$ interface has the larger thermodynamic driving force to react (**Figure 2c**). $BaCO_3$ decomposition is reported to have a substantial activation barrier of 305 kJ/mol [32], and the thermodynamic driving forces for all Y_2O_3-$BaCO_3$-CuO interfacial reactions have ΔG_{rxn} less negative than -100 kJ/mol up to 800 °C, which is evidently too small to overcome this kinetic barrier. These poor reaction kinetics, coupled with a small thermodynamic driving force, underlie the slow synthesis of YBCO when starting from a $BaCO_3$ precursor.

The fast formation of YBCO when starting from BaO_2 originates from the large thermodynamic driving force at the $BaO_2|CuO$ interface, which is ~200 kJ/mol larger than at the $BaCO_3|CuO$ interface at 600 °C. We previously demonstrated in the synthesis of Na_xMO_2 ($M = $ Co, Mn) that the first phase to form in an interfacial reaction is the compound with the largest compositionally unconstrained reaction energy from the precursors [10]. Here, our results in the

YBCO system provide further evidence for this theory. We calculate that $Ba_2Cu_3O_6$ has the largest reaction energy to form at the $BaO_2|CuO$ interface, and indeed this is the first observed ternary phase, which is accompanied by evolution of O_2 gas. Between 600 °C and 850 °C, $Ba_2Cu_3O_6$ decomposes to form $BaCuO_2$ and CuO (**Figure 2b**). The preferential reactivity of the $BaO_2|CuO$ interface—instead of the $Y_2O_3|BaO_2$ or $Y_2O_3|CuO$ interfaces—provides another example that the first phase to form in an interfacial reaction is the phase with the largest thermodynamic driving force, and further suggests that when multiple competing interfaces exist, the interface with the most exergonic compositionally-unconstrained reaction energy will initiate the solid-state reaction.

Our approach here assumes that thermodynamics plays the dominant role in selecting which pairwise interface is most reactive, but kinetic considerations are also important. In previous studies of diffusion couples between metal-silicon and metal-metal interfaces, both reaction energies and interdiffusion rates governed initial phase formation[33-35]. Transport kinetics are in fact intimately coupled with thermodynamic considerations, as thermodynamic driving forces appear in Fick's first law as the chemical potential gradient. When different pairwise interfaces exhibit large differences in driving forces, as they do here in the Y_2O_3-BaO_2-CuO system, thermodynamic considerations are likely to dominate the relative kinetics of interdiffusion. However, when the thermodynamic terms are comparable between different interfaces, a more explicit treatment of diffusion kinetics cannot be avoided. Because transport arises from a combination of bulk, dislocation, and surface diffusion mechanisms, it is today challenging to compute the relative interdiffusion kinetics between different interfaces.

However, in the limit where reactions are thermodynamically controlled, our model offers a tractable way to anticipate which pairwise interface will be most reactive in a given precursor mixture, and which phase is most likely to form at those interfaces—information which is invaluable for synthesis planning.
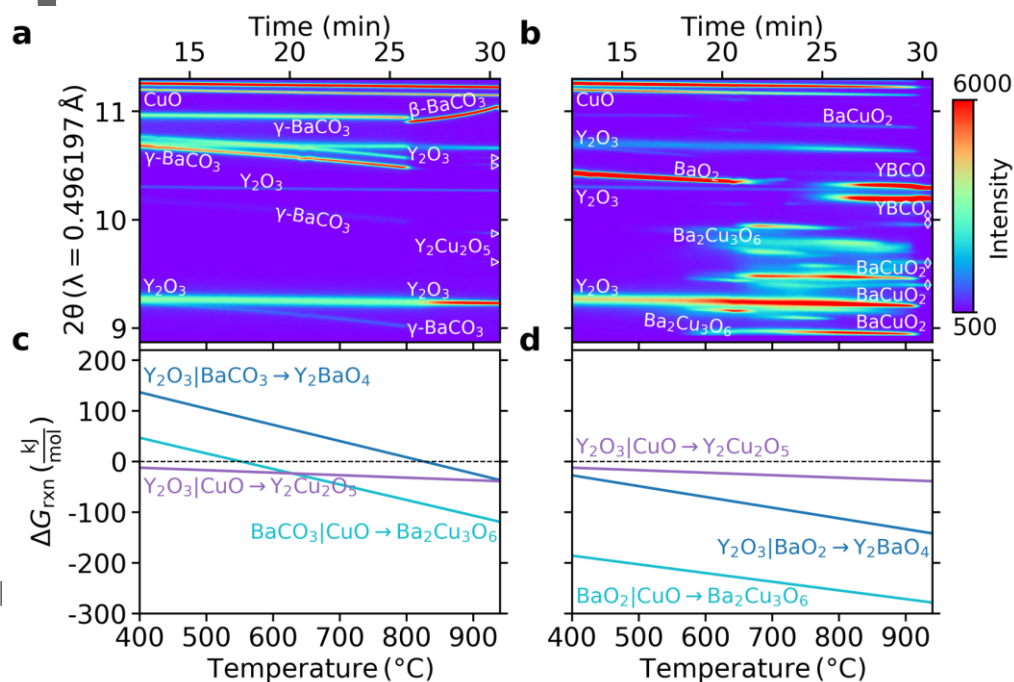
Figure 2. Phase evolution during YBCO synthesis compared to reaction thermodynamics. (a) *in situ* synchrotron XRD pattern for heating of the Y_2O_3 + $BaCO_3$ + CuO precursor mixture. The triangles mark peaks for $Y_2Cu_2O_5$. Individual XRD patterns at select temperatures are provided in **Figure S1**. **(b)** *in situ* synchrotron XRD pattern for heating of the Y_2O_3 + BaO_2 + CuO precursor mixture. Individual XRD patterns at select temperatures are provided in **Figure S2**. Mixed powders were heated in quartz tubes under air atmosphere at a heating rate of 30 °C/min. Diamonds markers indicate peaks for Y_2BaCuO_5. **(c)** Gibbs reaction energies for the lowest energy reactions at each interface in the Y_2O_3 + $BaCO_3$ + CuO precursor mixture. The reactions are $Y_2O_3|BaCO_3 = 1.5\ Y_2O_3 + 1.5\ BaCO_3 \rightarrow 1.5\ BaY_2O_4 + 1.5\ CO_2$; $Y_2O_3|CuO = 1.5\ Y_2O_3 + 3\ CuO \rightarrow 1.5\ Y_2Cu_2O_5$; $BaCO_3|CuO = 12/7\ BaCO_3 + 18/7\ CuO + 3/7\ O_2 \rightarrow 6/7\ Ba_2Cu_3O_6 + 12/7\ CO_2$, **(d)** Gibbs reaction energies for the lowest energy reactions at each interface in the Y_2O_3 + BaO_2 + CuO precursor mixture. The reactions are $Y_2O_3|BaO_2 = 2\ Y_2O_3 + 2\ BaO_2 \rightarrow 2\ BaY_2O_4 + O_2$, $Y_2O_3|CuO = 1.5\ Y_2O_3 + 3\ CuO \rightarrow 1.5\ Y_2Cu_2O_5$, $BaO_2|CuO = 2.4\ BaO_2 + 3.6\ CuO \rightarrow 1.2\ Ba_2Cu_3O_6 + 0.6\ O_2$. The coefficients of each reaction are normalized to be consistent with the

formation of 1 mol of $YBa_2Cu_3O_{6.5}$ in an atmosphere open to O_2. As such, the products of each reaction form 6 mol of non-oxygen atoms. See the **Supplementary Information** for more details.

Whereas *in situ* XRD measurements track the temperature-time-transformation evolution of the system, *in situ* SEM/DF-STEM provides direct spatiotemporal observation of the microstructural evolution during the solid-state reaction. We next monitored the synthesis of YBCO from Y_2O_3-BaO_2-CuO on a hot stage using *in situ* electron microscopy (SEM/DF-STEM: Hitachi HF5000). Although the *in situ* microscopy used here cannot identify crystal structure, the reaction conditions (temperature, heating rate, precursors) are similar to those characterized by *in situ* XRD (**Figure 2b**). One difference is that the *in situ* microscopy heating was conducted in vacuum as opposed to air, but we show in **Figure S3**, that this does not significantly affect the thermodynamic driving forces in the initial pairwise reactions. For this reason, we anticipate that the temperature-time-transformation progression between the two methods (XRD and electron microscopy) are comparable. We also characterize the elemental distribution in the sample using energy-dispersive X-ray spectroscopy (EDX) before and after the *in situ* microscopy experiment (our EDX instrument can only operate at room temperature). In **Figure 3a**, we show DF-STEM snapshots of the particles during heating along with EDX before and after heating. A video of this reaction is also provided as **Supplementary File 1**.

At room temperature, EDX shows that the three precursor powders are in intimate contact. Importantly, it is clear from EDX that all three potential pairwise interfaces (Y_2O_3|BaO_2, Y_2O_3|CuO, and BaO_2|CuO) exist in the sample. As the stage is heated to 500 °C, the initial BaO_2 and CuO precursors react at the BaO_2|CuO interface, which according to the *in situ* XRD

experiments, results in $Ba_2Cu_3O_6$. Meanwhile, the Y_2O_3 particle remains inert, as does its interface with BaO_2. From 650 °C to 800 °C, we observe the ejection of small bubble-like particles, which corresponds to the reaction: $Ba_2Cu_3O_6 \rightarrow 2\ BaCuO_2 + CuO + 0.5\ O_2$. In a separate *in situ* heating experiment, we confirm with SEM and EDX measurements that this initial reaction occurs strictly in the Ba-Cu-O subsystem (**Figure S4**). The observed reactivity of the $BaO_2|CuO$ interface and inertness of the Y_2O_3-containing interface aligns with our thermodynamic predictions from **Figure 2d**.

From **Figure 1b**, we calculated the total thermodynamic driving force of $0.5\ Y_2O_3 + 2\ BaO_2 + 3\ CuO \rightarrow YBa_2Cu_3O_{6.5} + O_2$ to be approximately −200 kJ/mol. For the formation of $BaCuO_2$, we calculate a reaction energy of −130 kJ/mol ($2\ BaO_2 + 2\ CuO \rightarrow 2\ BaCuO_2 + O_2$), meaning that ~2/3rd of total reaction driving force is consumed before Y_2O_3 becomes involved in the reaction. Only ~70 kJ/mol remain to drive the reaction to form YBCO. This is more or less comparable to the overall reaction energy from Y_2O_3, $BaCO_3$ and CuO (**Figure 1b**), indicating this thermodynamic driving force does not account for the quick formation of YBCO when BaO_2 is used. Thus, we anticipate kinetic selection to play the primary role in the formation of the next phase. Indeed, this kinetic mechanism is provided by the melting of $BaCuO_2$ and CuO at ~900 °C. This liquid Ba-Cu-O melt is then rapidly consumed into the Y_2O_3 particle to form YBCO. In the EDX taken after the experiment, the morphology of the Y region remains similar to the beginning of the experiment, but now Ba and Cu signals are found in the final particle.

In **Figure 3b**, we overlay the observed phase evolution sequence onto the pseudo-binary BaO_2-CuO slice [36] of the overall Y_2O_3-BaO_2-CuO phase diagram to reveal how the BaO_2

precursor enables rapid YBCO synthesis. The first reaction occurs before 500 °C and proceeds at the BaO_2|CuO interface to form $Ba_2Cu_3O_6$. This is consistent with our calculations in **Figure 2d**, where we found the BaO_2|CuO interface to be the most reactive among the three precursor interfaces and $Ba_2Cu_3O_6$ to be the phase with the largest driving force to form at this interface. Above 700°C, $Ba_2Cu_3O_6$ undergoes peritectoid decomposition into $BaCuO_2$ and CuO, which was observed as the ejection of small bubble-like particles in **Figure 3a**. $BaCuO_2$ and CuO are unreactive until the temperature is increased to their eutectic point at 890 °C, after which $BaCuO_2$ and CuO melt into one another. This liquid melt becomes a self-flux, providing fast kinetic transport of Ba and Cu into Y_2O_3 for the rapid formation of YBCO at the Y_2O_3|Ba-Cu-O(liquid) interface.

To verify the role of $BaCuO_2$ and the $BaCuO_2$|CuO eutectic in enabling rapid YBCO synthesis, we performed an additional *in situ* synthesis starting from Y_2O_3, $BaCuO_2$, and CuO, which similarly leads to rapid YBCO formation above ~890 °C (**Figure S5**). A deviation between the total mass of crystalline phases and the thermogravimetric measurement of the total sample mass that precedes rapid YBCO formation again confirms that a liquid phase mediates YBCO formation.

If one consults the Y_2O_3-CuO or Y_2O_3-BaO_2 phase diagrams [37], the lowest liquidus temperatures in these systems are ≥ 1095 °C, which is above the temperature at which YBCO decomposes (1006 °C) [38]. BaO_2 therefore plays a crucial role in directing the phase evolution through the pseudo-binary BaO_2-CuO subsystem—where a low-temperature liquid self-flux provides the fast diffusion kinetics that facilitates the formation of YBCO in 30 minutes. This is in

contrast to when $BaCO_3$ is used as the Ba source, where the slow decomposition reaction kinetics at the $BaCO_3$|CuO interface forces the overall reaction to proceed through the Y_2O_3-CuO subsystem, and a high liquidus temperature of 1095 °C obstructs any liquid-mediated transport kinetics for YBCO formation [37].

Although the overall reaction energies shown in **Figure 1b** suggest that the larger thermodynamic driving force is why a reaction with the BaO_2 precursor proceeds more quickly than with $BaCO_3$, we emphasize here that the magnitude of the overall reaction energy is not the origin of the fast synthesis time. Instead, it is the initial selection of the BaO_2-CuO subsystem, where there is a low-temperature eutectic below the decomposition temperature of YBCO, that enables rapid YBCO synthesis by forming a self-flux. This finding highlights the need to consider computations beyond the phase stabilities of the target or overall reaction energies in order to obtain mechanistic insights into the reaction pathways by which phases can evolve during synthesis.
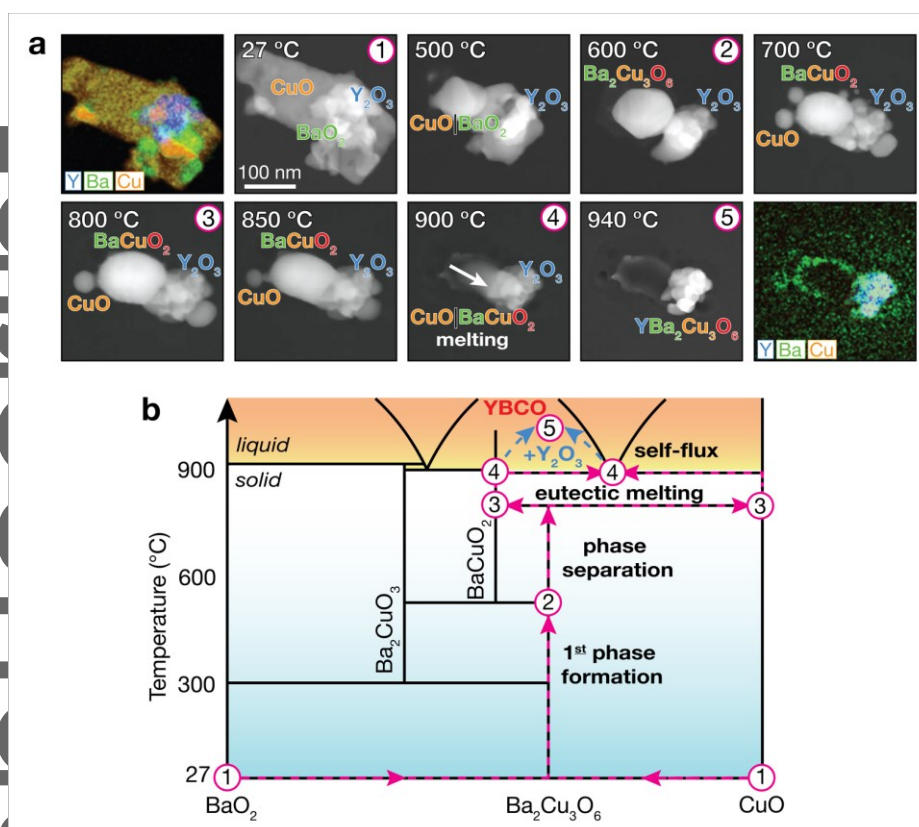
**Figure 3.** *In situ* microscopy of YBCO formation from Y_2O_3, BaO_2, and CuO particles and the observed phase evolution sequence mapped onto the BaO_2-CuO phase diagram. **(a)** *In situ* DF-STEM and EDX images show the heating of 0.5 Y_2O_3 + 2 BaO_2 + 3 CuO from 27 °C to 940 °C at 30 °C/min. The markers in the upper right corner of select panels are for comparison to panel B. A video of the reaction is provided in **Supplementary File 1**. *In situ* SEM and EDX for a shorter run to capture the initial formation of $Ba_2Cu_3O_6$ is also provided in **Figure S4**. **(b)** Observed phase evolution sequence in the context of the pseudo-binary phase diagram for BaO_2-CuO, adapted from Ref. [36].

Upon cooling the sample down from 940 °C at a rate of 5 °C/min, *in situ* XRD shows in **Figure 4** a structural transition from tetragonal to orthorhombic YBCO at 620 °C, indicating the uptake of ambient O_2 into $YBa_2Cu_3O_6$ to form $YBa_2Cu_3O_{6+x}$, consistent with reports from the literature [39, 40]. The synthesized product exhibits a strong diamagnetic signal below 77 K (**Figure 4c**), indicating the successful synthesis of superconducting YBCO. From a thermodynamic

perspective, it is well-characterized that $YBa_2Cu_3O_{6+x}$ is metastable at low temperature with respect to decomposition [41] by the reaction:

$$YBa_2Cu_3O_{6.5} + 0.5\ O_2 \rightarrow 0.5\ Y_2O_3 + 1\ Ba_2Cu_3O_6 \qquad \Delta G_{rxn} \approx -100\ kJ/mol\ at\ 27\ °C$$
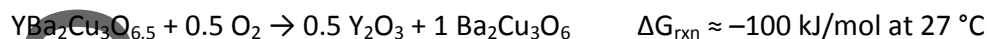
However, this solid-state decomposition is kinetically limited during cooling. On the other hand, oxygen diffusion is highly mobile in the YBCO framework [42, 43], indicating that this final topotactic uptake of O_2 gas at the YBCO|O_2 interface is a kinetically mediated non-equilibrium reaction.
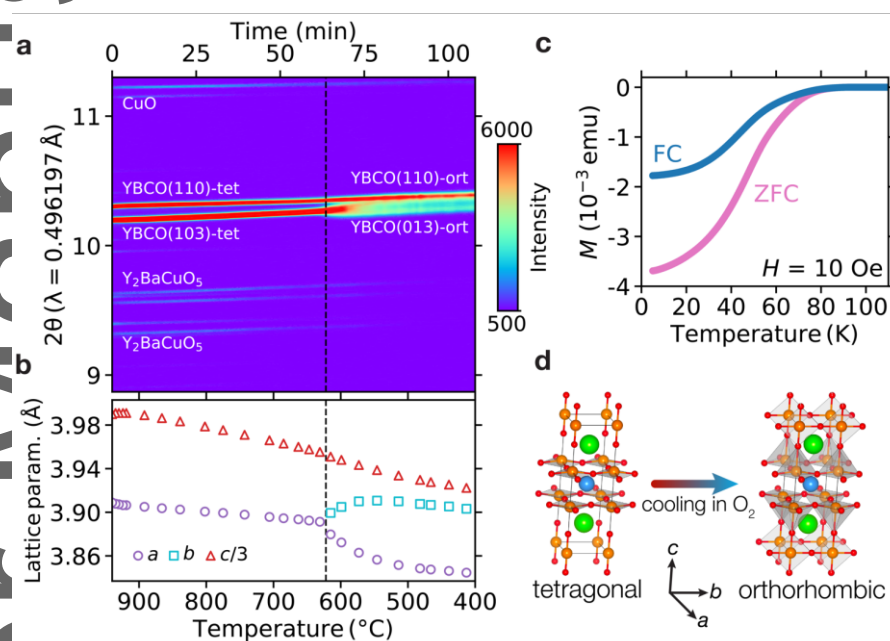
Figure 4. Topotactic O₂ uptake and phase transition during slow cooling. (**a**) *in situ* synchrotron XRD pattern for cooling of Y_2O_3 + BaO_2 + CuO precursor from 940 °C to 400 °C at 5 °C/min. "tet" refers to the tetragonal structure and "ort" to the orthorhombic structure. (**b**) Changes in lattice parameters during cooling. (**c**) Magnetic susceptibility of synthesized YBCO exhibiting superconductivity above liquidus nitrogen temperature. (**d**) The tetragonal and orthorhombic crystal structures for YBCO, where blue spheres are Y, green are Ba, orange are Cu, and red are O.

In **Figure 5**, we summarize how phase evolution during YBCO synthesis can be understood as a sequence of pairwise reactions that result from an interplay between thermodynamics and kinetics. The initial mixture of three precursors—Y_2O_3, BaO_2 and CuO—produces three possible reactive interfaces. We calculated in **Figure 2d** that the BaO_2|CuO interface possesses the largest thermodynamic driving force to react, and predicted $Ba_2Cu_3O_6$ to be the first reaction intermediate, which was confirmed by *in situ* XRD (**Figure 2b**) and *in situ* electron microscopy (**Figure 3a**, **Figure S4**). The formation of $Ba_2Cu_3O_6$ below 600 °C consumes ~2/3rd of the overall reaction driving force, meaning the ensuing reactions necessarily occur with smaller driving forces. Using *in situ* DF-STEM we observed that after the peritectoid decomposition of $Ba_2Cu_3O_6$ into $BaCuO_2$ + CuO, there is no further phase evolution in the system until the formation of a eutectic melt at the $BaCuO_2$|CuO interface. This liquid melt serves as a self-flux, providing fast Ba and Cu transport into the thus-far immobile Y_2O_3, forming $YBa_2Cu_3O_6$ (**Figure 3**). Finally, fast topotactic oxygen uptake at the $YBa_2Cu_3O_6$|O_2 interface upon cooling yields the superconducting $YBa_2Cu_3O_{6+x}$ phase (**Figure 4**), which persists kinetically as a metastable phase to room temperature, instead of decomposing to the equilibrium Y_2O_3 + $Ba_2Cu_3O_6$ phases.
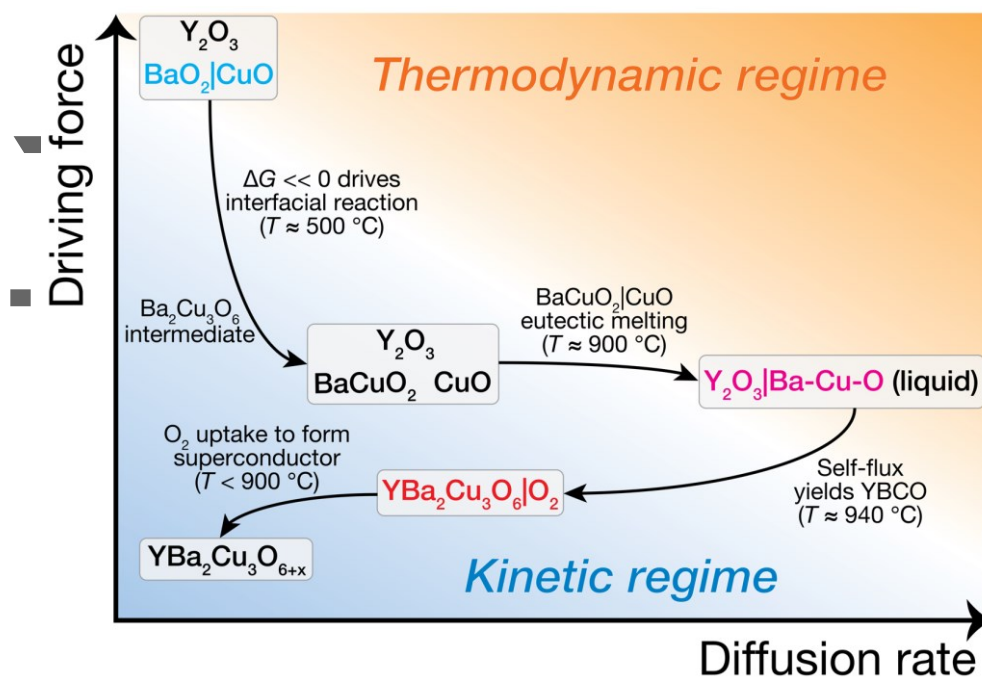
Figure 5. Phase evolution pathway for the formation of YBCO dictated by sequential pairwise reactions. The YBCO synthesis pathway is shown here along two qualitative axes – the thermodynamic driving force to form new phases along the vertical axis and the diffusion rate of reactive species along the horizontal axis. Within this framework, we understand reaction events occurring in either a thermodynamic regime, where driving forces or diffusion rates are sufficiently high that equilibrium products are observed, or a kinetic regime, where ion transport is sufficiently slow or driving forces sufficiently small such that the system becomes unreactive or non-equilibrium products are formed.

Our investigation here provides a general conceptual framework to approach the solid-state synthesis of complex multicomponent ceramics. A ceramic synthesis reaction that begins from N precursors will exhibit $_NC_2$ pairwise reaction interfaces. We showed here that in the early stages of synthesis, when thermodynamic driving forces are large, the first reaction will occur between the two precursors with the largest compositionally unconstrained reaction driving force. This initial reaction interface determines which pseudo-binary subsystem the ensuing phase evolution proceeds from, and we showed that this initial interface can be anticipated

from *ab initio* calculations. For YBCO, starting with a BaO_2 precursor leads to a large driving force to form $Ba_2Cu_3O_6$ at the $BaO_2|CuO$ interface; whereas starting from the traditional $BaCO_3$ precursor results in slow $BaCO_3$ decomposition kinetics, forcing the reaction through the Y_2O_3-CuO subsystem, where slow diffusion kinetics means manual regrinding is necessary to reintroduce interfaces between unfinished reaction intermediates.

In general, the replacement of oxide/carbonate precursors with peroxides may be an effective way to redirect the synthesis of multicomponent materials through different subsystems. In **Figure S6**, we show that the energy required to disproportionate alkali(ne) peroxides is generally less than their corresponding oxides/carbonates. By thoughtfully choosing the starting precursors[27, 44] to control which pairwise interface is the most reactive, one can deliberately direct phase evolution through whichever pseudo-binary subsystem exhibits the best kinetic pathway to the target material. Today, it remains difficult to anticipate which kinetic mechanisms are available in a given subsystem, especially when thermodynamic driving forces are similar between different interfaces. In the near term, *in situ* characterization remains the most productive approach for rationally designing solid-state synthesis recipes. In the future, a theoretical framework that embeds nucleation, diffusion, and crystal growth kinetics within a thermodynamic description of sequential pairwise reactions will pave the way towards a complete computational platform for predictive solid-state ceramic synthesis.

WILEY-VCH

Methods

In-situ synchrotron powder X-ray diffraction

Y$_2$O$_3$ (>99.9%, Kojundo Kagaku), BaCO$_3$ (>99.9 %, Kojyundo Kagaku), BaO$_2$ (>80%, Jyunsei Kagaku), CuO (>99%, Wako Chemical) were weighed in a molar ratio of for Y/Ba/Cu =1/2/3, and loaded into a zirconia pot with zirconia balls with a diameter of 4 mm. The starting materials were mechanochemically milled by planetary ball milling for 3 h over 150 rpm. The mixed powder was loaded into a quartz capillary with a diameter of 0.3 mm.

The change in crystalline phases were examined using synchrotron powder X-ray diffraction at the *BL02B2* beamline of *SPring-8* (proposal numbers 2019A1101, 2019B1195 and 2020A1096). The quartz capillary with powder mixture was settled in a furnace in air atmosphere. Heating started after setting in the furnace operated at 100 °C at the heating rate of 30 °C /min till 940 °C. The sample kept 10 min at 940 °C and then started cooling at 5 °C /min till 400 °C. The diffraction data of 2θ range from 8.9° to 15.5° with a step of 0.02° were collected using a high-resolution one-dimensional semiconductor detector (MYTHEN)[45]. The wavelength of the radiation beam was determined using a CeO$_2$ standard. Rietveld refinement was performed by RIETAN-FP[46], and the crystal structure was visualized using VESTA software.[47]

In-situ TEM measurement

In an Ar-filled glove box, BaO$_2$ powder (>80%, Jyunsei Kagaku) was mechanochemically milled by planetary ball milling for 8 h over 150 rpm. The powder was sieved to remove particles

20

larger than 20 μm. In ambient atmosphere, Y_2O_3 (>99.9%, Kojundo Kagaku), CuO nanopowder (>99%, Alderich), and above BaO_2 powder were weighed in a molar ratio of for Y/Ba/Cu =1/2/3, and loaded again into a zirconia pot with φ 4 mm zirconia balls. The powder was mechanochemically mixed by planetary ball milling for 3 h over 150 rpm. The sample was dispersed in dehydrate ethanol, and ultrasonicated. This suspension was dropped onto a silicon nitride TEM grid.

Morphology and compositional change were observed by transmission electron microscopy (TEM: HF-5000 Hitachi High-Tech Corporation). The accelerate voltage was 200 kV, and pressure was approximately 2×10^{-5} Pa. The sample was initially heated at 300 °C, and then heated till 940 °C at 30 °C /min. The apparatus allows to record three images simultaneously: scanning electron microscope (SEM), bright-field scanning transmission electron microscopy (BF-STEM), and dark-field scanning transmission electron microscopy (DF-STEM) images. Before and after heating the sample, compositional distribution was examined by energy-dispersive X-ray (EDX) mapping at room temperature.

Magnetization measurement

Magnetization was measured using a superconducting quantum interference device (SQUID) magnetometer (Quantum Design MPMS-3) with an applied field of 10 *Oe*, in order to check Meissner effect of synthesized sample.

Computational

Standard Gibbs formation energies, $\Delta G^{\circ}_{f}(T)$, for gaseous species were obtained from NIST [48]. To account for the synthesis atmosphere (air), Gibbs formation energies of a given gaseous species, $\Delta G^{\circ}_{f,i}(T)$, were obtained as:

$$\Delta G_{f,i}(T) = \Delta G^{o}_{f,i}(T) + RT ln(p_i)$$

where R is the gas constant and p_i approximates the activity coefficient of gaseous species, *i*. The only gaseous species evolved or consumed in reactions discussed in this work are O_2 and CO_2, where p_{O2} was taken to be 0.21 atm and p_{CO2} = 0.0004 atm.

For solid-state compounds, formation enthalpies (at 0 K) were obtained with density functional theory (DFT), utilizing the SCAN meta-GGA density functional [30]. Each structure was obtained from the Materials Project database [49] and optimized using the Vienna Ab Initio Simulation Package (VASP) [50] and the projector augmented wave (PAW) method [51], a plane-wave energy cutoff of 520 eV, and 1000 k-points per reciprocal atom.

Standard Gibbs formation energies, $\Delta G^{\circ}_{f}(T)$, for each solid-state compound were then obtained by combining the DFT-calculated formation enthalpies, the machine-learned descriptor introduced in [31], and experimental Gibbs energy data for elemental phases as described in [31]. The activity of all solid phases was taken to be 1, so $\Delta G_{f}(T) = \Delta G^{\circ}_{f}(T)$.

Gibbs reaction energies, $\Delta G_{rxn}(T)$ were obtained as:

$$\Delta G_{rxn}(T) = \sum_{products} \Delta G_f(T) - \sum_{reactants} \Delta G_f(T)$$

The coefficients of each reaction were selected such that 6 moles of non-oxygen atoms appear in the product side of each reaction. This was done to normalize the comparison of $\Delta G_{rxn}(T)$ across a diverse set of reactions, and because the reacting mixture was assumed to exchange freely with O_2 in the synthesis atmosphere.

Supporting Information

Supporting Information is available from the Wiley Online Library or from the author.

Acknowledgements

References

[1]   W. D. Kingery, H. K. Bowen, D. R. Uhlmann, *Introduction to Ceramics, 2nd Edition*, Wiley-Blackwell, Hoboken, New Jersey 1976.

[2]   M. G. Kanatzidis, K. R. Poeppelmeier, S. Bobev, A. M. Guloy, S.-J. Hwu, A. Lachgar, S. E. Latturner, S. E. Raymond, D.-K. Seo, S. C. Sevov, A. Stein, B. Dabrowski, J. E. Greedan, M. Greenblatt, C. P. Grey, A. J. Jacobson, D. A. Keszler, J. Li, M. A. Subramanian, Y. Xia, T. Cagin, U. Häussermann, T. Hughbanks, S. D. Mahanti, D. Morgan, D.-K. Seo, N. A. Spaldin, W. E. Buhro, D. E. Giammar, J. A. Hollingsworth, D. C. Johnson, A. J. Nozik, X. Peng, R. L. Bedard, N. E. Brese, G. Cao, S. S. Dhingra, C. R. Kagan, D. B. Mitzi, M. J. Geselbracht, G. C. Lisensky, M. W. Lufaso, P. A. Maggard, O. K. Michael, A. P. Wilkinson, H.-C. zur Loye, T. Egami, J. E. Greedan, J. P. Hodges, J. D. Martin, J. B. Parise, B. H. Toby, T. A. Vanderah, P. C. Burns, J. Y. Chan, A. E. Meyer, C. B. Murray, A. P. Ramirez, M. D. Ward, L. Yu, M. A. Alario-Franco, P. D. Battle, T. Bein, C. L. Cahill, P. S. Halasyamani, A. Maignan, R. Seshadri, *Prog. Solid State Chem.* **2008**, *36*, 1.

[3]   A. R. West, *Solid State Chemistry and its Applications*, Wiley, 2014.

[4]   M. H. Nielsen, S. Aloni, J. J. De Yoreo, *Science* **2014**, *345*, 1158.

[5]   A. J. Martinolich, J. A. Kurzman, J. R. Neilson, *J. Am. Chem. Soc.* **2016**, *138*, 11031.

[6]   Z. Jiang, A. Ramanathan, D. P. Shoemaker, *J. Mater. Chem. C* **2017**, *5*, 5709.

[7]   A. S. Haynes, C. C. Stoumpos, H. Chen, D. Chica, M. G. Kanatzidis, *J. Am. Chem. Soc.* **2017**, *139*, 10814.

[8]   H. He, C.-H. Yee, D. E. McNally, J. W. Simonson, S. Zellman, M. Klemm, P. Kamenov, G. Geschwind, A. Zebro, S. Ghose, J. Bai, E. Dooryhee, G. Kotliar, M. C. Aronson, *PNAS* **2018**, *115*, 7890.

[9]   H. Kohlmann, *Eur. J. Inorg. Chem.* **2019**, *2019*, 4174.

[10]   M. Bianchini, J. Wang, R. J. Clement, B. Ouyang, P. Xiao, D. Kitchaev, T. Shi, Y. Zhang, Y. Wang, H. Kim, M. Zhang, J. Bai, F. Wang, W. Sun, G. Ceder, *Nat Mater* **2020**.

[11]   S. P. Ong, L. Wang, B. Kang, G. Ceder, *Chem. Mater.* **2008**, *20*, 1798.

[12]   W. Sun, S. T. Dacek, S. P. Ong, G. Hautier, A. Jain, W. D. Richards, A. C. Gamst, K. A. Persson, G. Ceder, *Sci. Adv.* **2016**, *2*, e1600225.

[13]   C. J. Bartel, A. W. Weimer, S. Lany, C. B. Musgrave, A. M. Holder, *npj Computational Materials* **2019**, *5*, 4.

[14]   A. Narayan, A. Bhutani, S. Rubeck, J. N. Eckstein, D. P. Shoemaker, L. K. Wagner, *Phys. Rev. B* **2016**, *94*.

[15]   M. Jansen, *Angew. Chem. Int. Ed.* **2002**, *41*, 3746.

[16]   A. Miura, H. Ito, C. J. Bartel, W. Sun, N. C. Rosero-Navarro, K. Tadanaga, H. Nakata, K. Maeda, G. Ceder, *Materials Horizons* **2020**, *7*, 1310.

[17]   F. J. DiSalvo, *Science* **1990**, *247*, 649.

[18]   A. Sleight, *Synthesis of Oxide Superconductors*, Vol. 44, 1991.

[19]   J. R. Chamorro, T. M. McQueen, *Acc. Chem. Res.* **2018**, *51*, 2918.

[20]   D. L. M. Cordova, D. C. Johnson, *ChemPhysChem* **2020**, *21*, 1345.

[21]   M. Wu, J. Ashburn, C. Torng, P. Hor, R. Meng, L. Gao, Z. Huang, Y. Wang, C. Chu, *Phys. Rev. Lett.* **1987**, *58*, 908.

[22]   S. Hikami, T. Hirai, S. Kagoshima, *Jpn. J. Appl. Phys.* **1987**, *26*, L314.

[23]   R. J. Cava, B. Batlogg, R. B. van Dover, D. W. Murphy, S. Sunshine, T. Siegrist, J. P. Remeika, E. A. Rietman, S. Zahurak, G. P. Espinosa, *Phys. Rev. Lett.* **1987**, *58*, 1676.

[24]   P. Grant, in *New Scientist*, New Scientist Ltd., London 1987, 36.

[25]   C. A. Costa, M. Ferretti, C. L. Olcese, M. R. Cimberle, C. Ferdeghini, G. L. Nicchiotti, A. S. Siri, C. Rizzuto, *J. Cryst. Growth* **1987**, *85*, 623.

[26]   B. D. Fahlman, *J. Chem. Educ.* **2001**, *78*, 1182.

[27]   X. Jia, A. Lynch, Y. Huang, M. Danielson, I. Lang'at, A. Milder, A. E. Ruby, H. Wang, S. A. Friedler, A. J. Norquist, J. Schrier, *Nature* **2019**, *573*, 251.

[28]   J. L. Jorda, T. K. Jondo, *J. Alloys Compd.* **2001**, *327*, 167.

[29]   O. Kononova, H. Huo, T. He, Z. Rong, T. Botari, W. Sun, V. Tshitoyan, G. Ceder, *Scientific Data* **2019**, *6*, 203.

[30]   J. Sun, A. Ruzsinszky, J. P. Perdew, *Phys. Rev. Lett.* **2015**, *115*, 036402.

[31]   C. J. Bartel, S. L. Millican, A. M. Deml, J. R. Rumptz, W. Tumas, A. W. Weimer, S. Lany, V. Stevanovic, C. B. Musgrave, A. M. Holder, *Nat Commun* **2018**, *9*, 4168.

[32]   I. Arvanitidis, D. Siche, S. Seetharaman, *Metall. Mater. Trans. B* **1996**, *27*, 409.

[33]   R. M. Walser, R. W. Bené, *Appl. Phys. Lett.* **1976**, *28*, 624.

[34]   R. Pretorius, A. M. Vredenberg, F. W. Saris, R. de Reus, *J. Appl. Phys.* **1991**, *70*, 3636.

[35]   C. C. Theron, O. M. Ndwandwe, J. C. Lombaard, R. Pretorius, *Mater. Chem. Phys.* **1996**, *46*, 238.

[36]   G. F. Voronin, S. A. Degterov, *J. Solid State Chem.* **1994**, *110*, 50.

[37]   B.-J. Lee, D. N. Lee, *J. Am. Ceram. Soc.* **1991**, *74*, 78.

[38]   W. Wong-Ng, L. P. Cook, *J. Res. Natl. Inst. Stand. Technol.* **1998**, *103*, 379.

[39]   J. D. Jorgensen, M. A. Beno, D. G. Hinks, L. Soderholm, K. J. Volin, R. L. Hitterman, J. D. Grace, I. K. Schuller, C. U. Segre, K. Zhang, M. S. Kleefisch, *Phys. Rev. B* **1987**, *36*, 3608.

[40]   R. P. Stoffel, C. Wessel, M. W. Lumey, R. Dronskowski, *Angew. Chem. Int. Ed. Engl.* **2010**, *49*, 5242.

[41]   E. L. Brosha, P. K. Davies, F. H. Garzon, I. D. Raistrick, *Science* **1993**, *260*, 196.

[42]   N. Chen, S. J. Rothman, J. L. Routbort, K. C. Goretta, *J. Mater. Res.* **1992**, *7*, 2308.

[43]   D. de Fontaine, G. Ceder, M. Asta, *Nature* **1990**, *343*, 544.

[44]   T. He, W. Sun, H. Huo, O. Kononova, Z. Rong, V. Tshitoyan, T. Botari, G. Ceder, *Chem. Mater.* **2020**, *32*, 7861.

[45]   S. Kawaguchi, M. Takemoto, K. Osaka, E. Nishibori, C. Moriyoshi, Y. Kubota, Y. Kuroiwa, K. Sugimoto, *Rev. Sci. Instrum.* **2017**, *88*, 085111.

[46]   F. Izumi, K. Momma, *Solid State Phenom.* **2007**, *130*, 15.

[47]   K. Momma, F. Izumi, *J. Appl. Crystallogr.* **2008**, *41*, 653.

[48]   M. W. Chase, *NIST-JANAF Thermochemical Tables, 4th Edition*, American Institute of Physics, 1998.

[49]   A. Jain, S. P. Ong, G. Hautier, W. Chen, W. D. Richards, S. Dacek, S. Cholia, D. Gunter, D. Skinner, G. Ceder, K. A. Persson, *APL Materials* **2013**, *1*, 011002.

[50]   G. Kresse, J. Hafner, *Phys. Rev. B* **1993**, *47*, 558.

[51]   G. Kresse, D. Joubert, *Phys. Rev. B* **1999**, *59*, 1758.

Multicomponent ceramics are often synthesized in a 'black-box' reactor, with little understanding of how multiple precursors evolve into a target material. We use *ab initio* modeling and *in situ* observations to interrogate the phase evolution of $YBa_2Cu_3O_{6+x}$ (YBCO), highlighting the critical role of precursor selection in designing kinetically favorable synthesis pathways.

Akira Miura*, Christopher J. Bartel, Yusuke Goto, Yoshikazu Mizuguchi, Chikako Moriyoshi, Yoshihiro Kuroiwa, Yongming Wang, Toshie Yaguchi, Manabu Shirai, Masanori Nagao, Nataly Carolina Rosero-Navarro, Kiyoharu Tadanaga, Gerbrand Ceder, Wenhao Sun*

Observing and modeling the sequential pairwise reactions that drive solid-state ceramic synthesis